Quantum Dots for Improved Single-Molecule Localization Microscopy

Jennifer M. Urban[†], Wesley Chiang[¥], Jennetta W. Hammond[§], Nicole M. B. Cogan[†], Angela Stout[§,] Rebeckah Burke[†], Harry A. Stern[#,] Harris A. Gelbard[§*], Bradley L. Nilsson[†*], and Todd D. Krauss[†,£*]

[†]Department of Chemistry, [£]The Institute of Optics, and the [#]Center for Integrated Research and Computing, University of Rochester, Rochester, New York 14627-0216, United States

[¥]Department of Biochemistry and Biophysics, [§]Center for Neurotherapeutics Discovery, Departments of Neurology, Pediatrics, Neuroscience and Microbiology and Immunology, University of Rochester Medical Center, Rochester, NY, 14642.

Keywords: STORM, super-resolution imaging, PALM, quantum dots, neuronal imaging

ABSTRACT Colloidal semiconducting quantum dots (QDs) have long established their versatility and utility for the visualization of biological interactions. On the single particle level quantum dots have demonstrated superior photophysical properties compared to organic dye molecules or fluorescent proteins, but it remains an open question as to which of these fundamental characteristics are most significant with respect to the performance of QDs for imaging beyond the diffraction limit. Here, we demonstrate significant enhancement in achievable localization precision in QD labeled neurons compared to neurons labeled with an organic fluorophore. Additionally, we identify key photophysical parameters of QDs responsible for this enhancement and compare these parameters to reported values for commonly used fluorophores for super-resolution imaging.

INTRODUCTION

In the past decade, fluorescence microscopy has been revolutionized through the development of super-resolution imaging techniques, which can produce optical images with resolvable features on the order of 10-100 nm, up to an order of magnitude beyond the limit established by diffraction.[1-10] Super-resolution microscopy typically involves the limiting of fluorescence from closely spaced fluorophores using either temporal[5, 6, 10, 11] or spatial[8, 9, 12-16] methods such that two closely spaced emitters in a diffraction limited area can be effectively isolated in a single fluorescence image frame.[14, 17-19] Stochastic optical reconstruction microscopy or STORM,[10] and its close relative photoactivatable localization microscopy (PALM),[5, 6] usually require fluorophores that can have their fluorescence intensity modulated "on" and "off" (*i.e.* intensity blinking). By collecting many fluorescence images wherein each image has a random subset of the fluorophores that are "on", the precise localization of each isolated emitter in each image frame can be subsequently determined. Combining the emitter localizations from every individual frame produces a final, super-resolution, reconstructed image.[5, 6, 10, 20]

The ideal super-resolution imaging fluorescent probes must satisfy a stringent set of criteria. These probes must be photostable during the collection of thousands of fluorescence images, have a high fluorescence quantum efficiency when in the "on" state, and have large optical absorption and emission cross sections resulting in a high brightness. Additionally, to use localization-based methods such as STORM/PALM in densely labeled scenes, probes must be able to have their fluorescence "blink" (either randomly or under photoactive or photochemical control). For most organic fluorophores and photoactivatable fluorescent proteins, achieving such properties often requires the use of oxygen-reducing buffer systems that can be cytotoxic over time, high laser excitation powers which can be both phototoxic to cells and result in an increase in the photobleaching rate, and/or the use of multiple excitation lasers which can be cost-prohibitive and complicated.[11, 21, 22]

Many of the shortcomings and complications associated with organic fluorophores and fluorescent dyes can be addressed by the superior fundamental photophysical properties of fluorescent nanoparticles. Recent studies have validated the applications of upconverting nanoparticles[23,24], nitrogen-vacancy color centers in nanodiamonds[25,26], and aggregation-induced emission[27,28] for patterned illumination methods such as stimulated emission depletion (STED). For localization-based methods, colloidal semiconductor quantum dots (QDs), as well as similar carbon[29] and polymer[30] based nanodots, are expected to achieve similar enhancements in resolution.[4, 12, 31-52] Like the aforementioned nanoparticles, quantum dots are extremely photostable and very bright emitters, allowing for the observance of fluorescence from individual QDs with high signal to noise from tens of minutes to hours.[37, 53-55] Also, broad absorption spectra coupled with narrow emission spectra allow for simpler spectral multiplexing using a single excitation source.[39, 56, 57]

Additionally, QDs naturally exhibit inherent fluorescence blinking, which eliminates the need for multiple photoactivation lasers or oxygen reducing buffers in order to enable the fluorescence intensity blinking required for super-resolution imaging applications.[58] QDs have also been proven to be viable fluorescent labels in many biological imaging applications including cancer cell detection, tumor drug delivery, cellular sensing, and molecular tracking.[59-71]

Recently, several proof of principle type reports have demonstrated the successful application of QDs to super-resolution imaging.[12, 40-43, 48, 49, 52] For example, QDs have been used to image biological structures whose dimensions, morphology, and/or locations are already well-documented, including microtubules,[40, 42, 48, 52, 72] vimentin filaments,[12] and cancer cells.[40, 41, 49, 50] However, few studies directly comparing QDs and organic fluorophores for super-resolution applications have been performed.[40, 42] Proving that QDs provide unique advantages for super-resolution imaging over more common fluorophores would open up a large window of opportunity for the widespread application of QDs to enable novel biological discoveries.

Herein we show that CdSe/CdS QDs functionalized with a neuropeptide, bradykinin (BK), are fundamentally superior STORM imaging probes than BK labeled with an organic fluorophore, 5-carboxytetra-methylrhodamine (TAMRA), termed BKQD and TAMRA-BK, respectively (see Figure S1). We compared super-resolution images of primary rat hippocampal neuronal cultures labeled using BKQD probes to images obtained using TAMRA-BK and found that BKQDs produced reconstructed STORM images with higher localization accuracy. Specifically, compared to the organic fluorophore, individual BKQDs have much higher signal to noise (SNR), are more photostable, and inherently "blink" at a faster rate. The extracted experimental values of these parameters for BKQD and TAMRA-BK were used to generate simulated photoluminescence images comprised of single and multiple emitters (see Movies S2-S7). From these images, we determined the exact role SNR blink rate and photostability play in the localization enhancement. Lastly, we compare these parameters with those published for commonly used fluorophores in single molecule localization microscopy (SMLM) to comment on the expected relative performance of QDs (Table S6) more generally.

EXPERIMENTAL METHODS

Peptide and quantum dot synthesis and modification. Bradykinin-functionalized, micelle-coated CdSe/CdS QDs (BKQDs) were prepared using oleic acid capped CdSe/CdS QDs with an emission maximum at 627 nm. CdSe/CdS QDs were synthesized according to variations of standard literature procedures.[73, 74] Their characterization data can be found in Figures S2-S4. The peptides C-PEG-Bradykinin (C-PEG-BK, Figure S1), Bradykinin (BK, Figure S1), and TAMRA-Bradykinin (TAMRA-BK, Figure S1) were synthesized via solid phase peptide synthesis, purified and quantified by reverse phase high performance liquid chromatography (HPLC, Table S1, Figures S5-S9), and characterized by matrix assisted laser desorption ionization time of flight mass spectrometry (MALDI-TOF MS, Table S2 and Figures S10-S12). Thiol-maleimide chemistry was utilized to conjugate C-PEG-BK to phosphatidylserine-PEG-maleimide (Figure S1).[75, 76] QDs were then encapsulated in micelles consisting of 60% BK-phosphatidylserine and 40% lipid-PEG using a protocol modified from Maiseyeu et al.[77] Detailed descriptions of all synthetic methods can be found in the Supporting Information.

Neuron culture and imaging. Cell cultures for all experiments consisted of primary mixed rat hippocampal neuronal and glial cultures at 18-21 days *in vitro* (DIV) grown on either glass or fused silica coverslips. For obtaining fluorescence images, neuronal cultures were treated with BKQDs or TAMRA-BK (Figure S1) for 15 minutes, fixed with paraformaldehyde, and imaged at 60 × magnification on a TIRF inverted optical microscope setup with 532 nm excitation. TAMRA-BK treated samples were imaged in a buffer containing glucose, glucose oxidase, cysteamine, and catalase as described by others[78, 79] while BKQD samples were imaged in PBS or neurobasal media. One thousand-frame movies were collected with a 25ms exposure time per frame. Further details on experimental procedures can be found in the Supporting Information.

Image reconstruction. In order to construct the super-resolution images, the ImageJ plugin QuickPALM was first used to provide the location of all fluorescent points that met a chosen minimum signal-to-noise cutoff.[80] Next, the results from QuickPALM were run through a custom analysis program ("csv2png", code given in SI) that removes any points not meeting a minimum resolution cutoff, calculates the error in x and y coordinates associated with each point, and then plots the localized points that meet these criteria as an opaque spot surrounded by a semi-transparent ellipse representing the uncertainty in centroid location.

Extraction of Photophysical Parameters. Localized points from the image reconstruction were used to identify individual fluorescent spots in the recorded movies of BKQDs and TAMRA-BK. From each of these spots, the mean PL of the bright pixels and the standard deviation of the background pixels was obtained per frame using ImageJ (Figure S13-15). The time series data from ImageJ were analyzed using a custom MATLAB (*v. 2020A*) script to extract the SNR, blink rate in blinks per second, and power law fits. Average values for SNR and blink rate were generated for BKQDs and TAMRA-BK, respectively, based on the output of each of these time traces (Figures S16-19). More detailed information about the computational analysis can be found in the Supporting Information.

Simulated Movies. Four pairs of simulation parameters were defined by combining permutations of the two average SNR and two average blink rates identified for

BKQDs and TAMRA-BKs (Table 1). These are termed as: *HighSNR-2bps, HighSNR-3bps, LowSNR-2bps, HighSNR-3bps*; blink rates were rounded to the nearest integer for naming simplicity. Each pair of SNR and blink rate parameters were then used to develop a set of simulated movies with a single emitter and a set of simulated movies with three well-overlapped emitters using a custom MATLAB script (see Figures S20-21 and Movie S2-S7). The ImageJ plugin QuickPALM was then used to localize the emitters in the movies, and the identified localizations were then analyzed using a custom MATLAB script to calculate the error from the true positions and the standard deviation (s), defined as $s = \frac{FWHM}{2.354}$, where FWHM is the full-width at half-maximum of the Gaussian used to fit the centroid positions (Figures S22-24). More specific details about the generation of movies and subsequent analysis can be found in the Supporting Information.

RESULTS AND DISCUSSION

BKQDs bind to neurons in vitro. Primary rat hippocampal neuronal glial cultures, as prepared, contain both neurons and astrocytes (Figure 1A), both of which express bradykinin receptors. Cultures were treated with BKQDs and observed via fluorescence imaging to ascertain whether the BKQDs successfully bound to cells. Fluorescence microscopy revealed many stationary BKQDs, and very few freely diffusing ones (Figure 1B and Movie S1), thus demonstrating that the BKQDs were bound to either cells or the coverslip. Single BKQDs exhibited the expected fluorescence intermittency (i.e. blinking), suggesting that micelle encapsulation and interactions with cell culture or coverslips did not have an adverse effect on the basic QD photophysical properties.

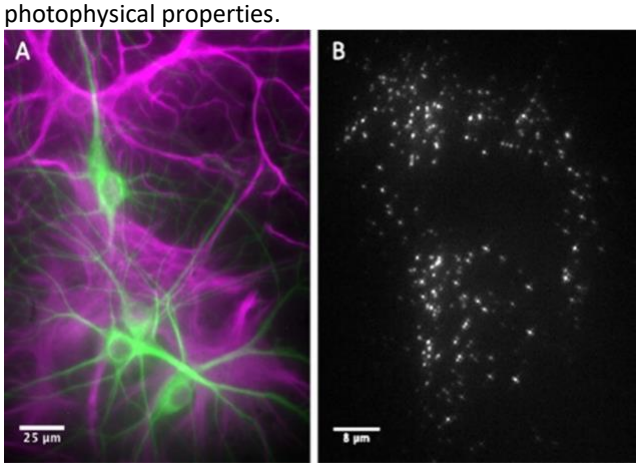

Figure 1. Example images of mixed neuronal glial cultures. A) Fluorescence image of a hippocampal neuronal glial culture highlighting the different cell types: astrocytes (purple) and neurons (green). B) Fluorescence image of BKQDs bound to neuronal cultures. An example of a single image frame obtained of a neuronal culture treated with 30 nM BKQDs for 15 minutes.

Super-resolution imaging: micelle-coated QDs are superior to TAMRA. Super-resolution images of neuronal cultures using BKQD probes were compared with images from a common organic fluorophore probe also used for STORM imaging, 5-carboxytetramethylrhodamine (TAMRA, Figure S1), as shown in Figures 2 and 3. Images of single QD fluorescence show bright, blinking BKQDs bound to cells with a typical SNR intensity ratio of up to 10. The first and last frames of a representative 25 second movie of the same area can be seen in Figure 2A and B, respectively. Comparing the first and last frame, we find that the overall intensity level of the QD fluorescence remains relatively unchanged over the acquisition time, proving the QDs to be photostable over the 25 s imaging time period, as expected (see Figure S14 for a representative fluorescence time trace of BKQDs during this imaging timeframe). The fluorescent spots highlighted in the yellow box of Figure 2A and B are shown magnified in Figure 2C and D. From these images it is difficult to tell if each spot corresponds to fluorescence from a single QD or multiple QDs, due to the relatively poor diffraction limited resolution. Using QuickPALM and the custom "csv2png" analysis program, the position of the QDs in this image was localized using a minimum SNR cutoff. Keeping only those points, a super-resolution image with a localization error of 50 nm, as shown in Figure 2E, shows QDs along the neuronal cell. The resulting reconstructed image of this area reveals that many of the seemingly single fluorescent spots in the original diffraction-limited images actually consist of multiple QDs in close proximity. Further, specific QDs can be localized with an accuracy of 30 nm (F) and even 25 nm (G), while still maintaining the overall pattern of the labeled BK receptors on the cell. Inevitably, as the allowable localization error decreases, more probes are discarded that do not satisfy the localization requirement, but a proper selection of a SNR cutoff adequately reproduces the underlying neuronal structure with BKQDs.

For comparison to BKQDs, neuronal cultures treated with TAMRA-BK were imaged in an oxygen reducing buffer at an excitation fluence four times what was used to image BKQDs (as required to obtain sufficient brightness and fluorescence intermittency). Compared to QDs, images of single TAMRA fluorescence show dimmer, less frequently blinking fluorescent spots bound to cells with signal-to-noise intensity ratios that only up to 6 (even at 4 times the fluence), and also photobleached more frequently. The first and last frames of a 25 s movie of TAMRA-BK labeled cells can be seen in Figure 3A and B, revealing the large degree of photobleaching experienced by the fluorophore during the experiment (also see Figure S15 for a representative fluorescence time trace of TAMRA-BK). The area highlighted in the yellow boxes of Figure 3A and B is shown magnified in Figure 3C and D, which was subsequently run through the localization algorithm as described for BKQDs. For image analysis and reconstruction, a 50 nm localization error cutoff proved to be the experimental limit for resolution of the image. Super-resolution processing revealed that many of the large fluorescent blurs in the original images were actually a result of multiple closely spaced fluorescent molecules (Figure 3E), similar to what

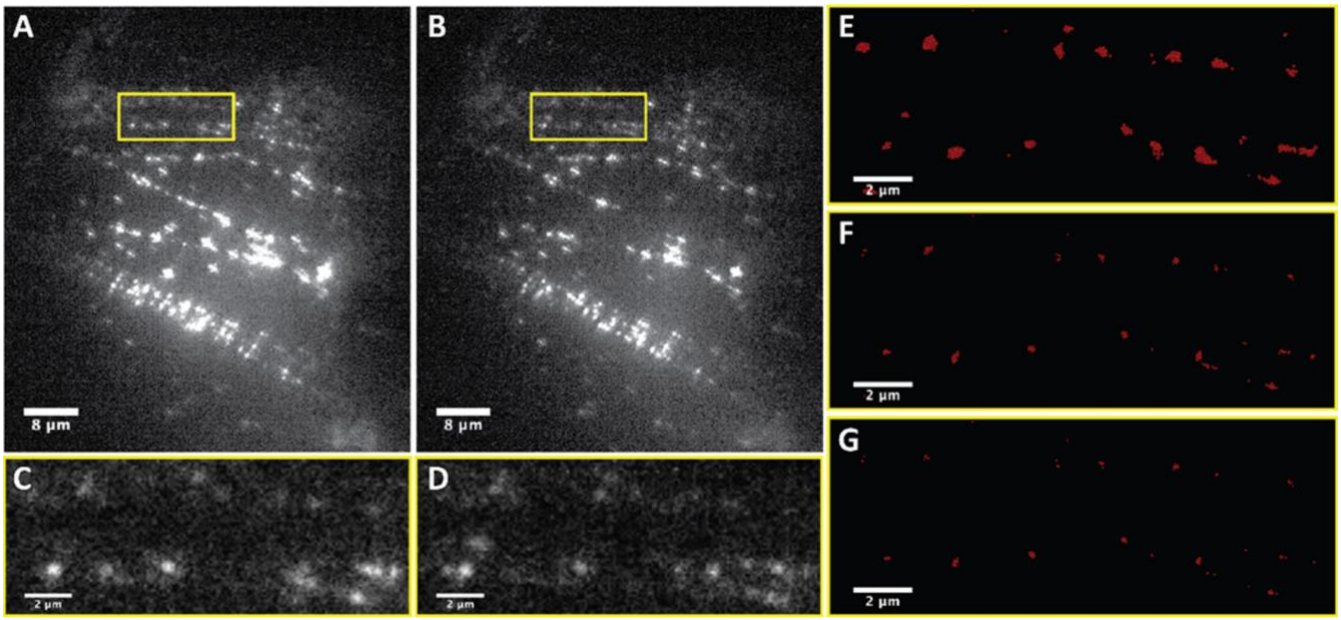

Figure 2. STORM imaging of BKQD treated neuronal cultures. A) Frame 1 out of 1000 from a movie of a neuronal culture treated with BKQDs. B) Frame 1000 from the same movie. C) Magnification of the area in the yellow box in A. D) Magnification of the area in the yellow box in B. E-G) Super-resolution reconstruction images of the area in the yellow boxes with localization precisions of E) 50 nm, F) 30 nm, and G) 25 nm showing successful localization at all resolution levels.

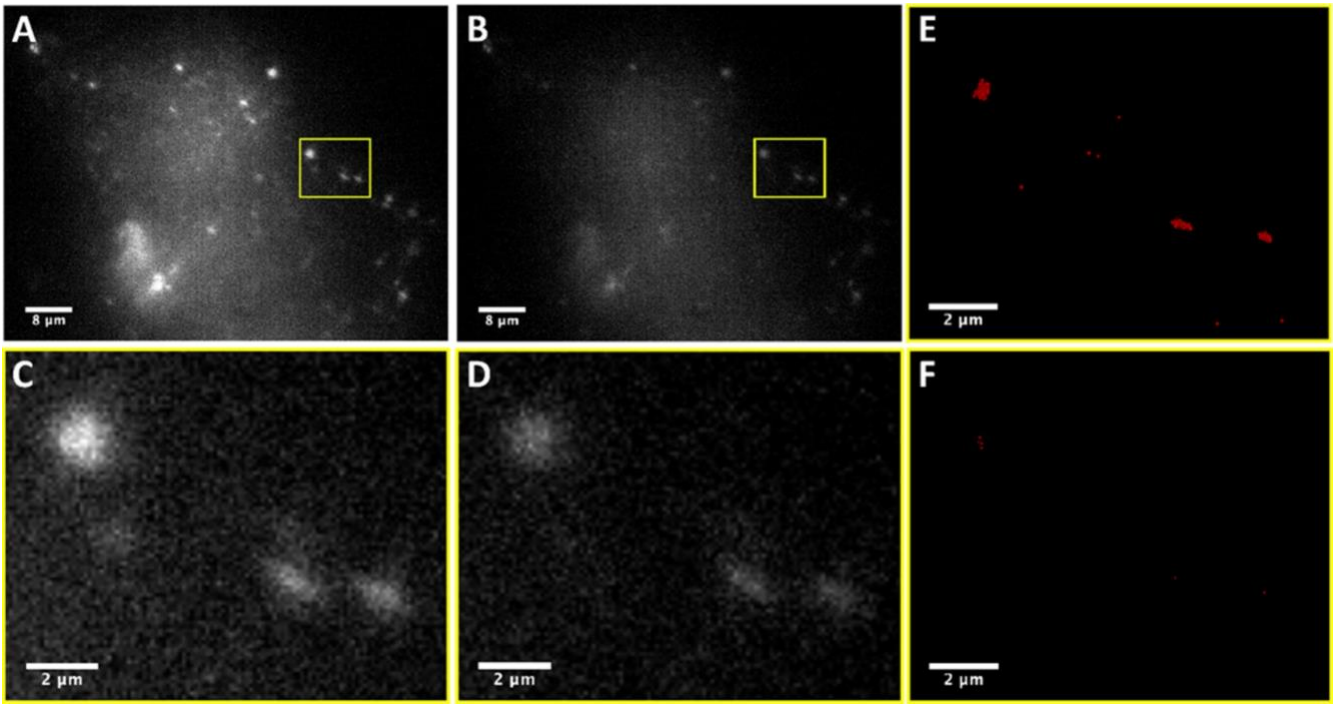

Figure 3. STORM imaging of TAMRA-BK treated neuronal cultures. A) Frame 1 out of 1000 of a movie of a neuronal culture treated with TAMRA-BK. B) Frame 1000 of the same movie showing significant photobleaching. C) Magnification of the area in the yellow box in A. D) Magnification of the area in the yellow box in B. E-F) Super-resolution reconstructed images of the area in the yellow box with localization precision at E) 50 nm showing successful localization and F) 30 nm showing very few localized points.

was observed with the BKQDs. However, TAMRA-BK molecules could only be localized at a 50 nm accuracy in reconstructed images, significantly worse than for QDs. At a 30 nm localization error cutoff significantly fewer TAMRA-BK probes were visible in the image, and thus structural information was lost (Figure 3F).

In addition to producing superior super-resolution images, QDs offered several practical advantages over the organic dye TAMRA. Like many other organic dyes, for STORM imaging TAMRA requires buffers that contain oxygen scavengers.[11, 79, 81, 82] This buffer has to be freshly prepared prior to use, and even the separate components cannot be stored for prolonged periods. From an experimental perspective, oxygen-scavenging buffers may confound paradigms to investigate pro-oxidative phenomena important to neurodegenerative disease. The

BKQD treated samples, on the other hand, were imaged in much simpler, physiologically relevant conditions: in PBS or neurobasal media. Also, optimizing proper imaging conditions for TAMRA was difficult due to its lower signal to noise ratio and lack of inherent blinking. The excitation power had to be balanced between providing a high signal to noise from the TAMRA and preventing rapid fluorophore bleaching. Finally, as shown in the SI, BKQDs are extremely photostable as expected. For example, once bound to cells and after cell fixation they remain fluorescent for at least a month (Figure S25). By contrast, the fluorescence intensity of TAMRA after one month fixed to cells was extremely low and the dye photobleached after a few seconds (Figure S26).

Interestingly, once localized, both the BKQDs and TAMRA-BK appear to be bound to the neurons in small clusters rather than as single entities. At first this seemed surprising, since we expected only a single probe to bind to each bradykinin receptor, however, this clustering could be explained by the well-established clustering of G-protein receptors.[83-87] The binding of bradykinin to its receptor(s) can result in receptor dimerization, receptors sequestering in caveolae, and/or receptor localization in lipid rafts.[83-87] Specifically, in PC-12 cells (a rat cell line that contains neuron-like cells), bradykinin B2 receptors have been observed clustering in lipid rafts as a result of ligand binding.[86, 87] The clustering of the QD and TAMRA probes likely indicates that one of these processes has occurred as a result of bradykinin binding.

Simulating Emitters: improved localization precision is primarily due to photostability and blink rate. By creating four unique emitters that mix the extracted SNR and blink rate of the BKQDs ($SNR \approx 5.5$, $blink\ rate \approx 3$) and TAMRA-BK ($SNR \approx 2.5$, $blink\ rate \approx 2$), we are able to parse out the exact role of each individual parameter in the improved localization precision of QDs compared to TAMRA (Table 1). In the recorded movies we also observe significant photobleaching in TAMRA-BK movies compared to BKQDs movies (Figures 2D and 3D). Thus, the length of the simulated movies are varied between 1000 frames and 3000 frames as a proxy for photostability; more measurements (i.e. frames) can be taken from an emitter resistant to photobleaching.

Table 1. SNR and blink rate parameters used for to create simulated movies

SNR	*Blinks per second (bps)*
~ 5.5	~ 3.0
~ 5.5	~ 2.0
~ 2.5	~ 3.0
~ 2.5	~ 2.0

To simulate a sparsely labeled sample (i.e. single-particle tracking), each of pair of parameters for SNR and blink rate were used to generate three replicates of 1000-frame simulations containing only a single emitter (see Movies S2-S5); individual emitters are easily resolved from one another in sparsely labeled samples. Using the ImageJ QuickPALM plugin, reconstruction images are generated corresponding where an emitter was localized in each frame; the more frequently the emitter was localized within a pixel, the more intense the shade of green (Figure 4). Using MATLAB, a 2D Gaussian is fit to the QuickPALM outputs to identify the centroid position for each single emitter simulation (see Figure S22 and Table S3). Grouping the results either by SNR or blink rate, the average localized centroid position and standard deviation ($s_{x,y} = \frac{FWHM_{x,y}}{2.354}$) are calculated for each parameter – High SNR, Low SNR, 3bps, or 2bps – and compare this to the true position of the simulated emitter (Table 2). Unsurprisingly, in a single emitter scenario SNR is the dominating factor in both localization accuracy $|Err_{x,y}|$, defined as the distance from the true position, and localization precision, which is dependent on $s_{x,y}$. As defined by eq 1, localization error $\sigma_{x,y}$ is approximately proportional to the standard deviation.[41]

$$\sigma_{x,y} = \sqrt{\frac{s_{x,y}^2}{N} + \frac{a}{12N} + \frac{8\pi s_{x,y}^4 b^2}{a^2 N^2}} \qquad (1)$$

Thus, a narrower Gaussian fit, corresponding to smaller $s_{x,y}$, for the localization of the centroid results in a reduced error, or increased localization precision. As seen in Figure 4, the simulations of "high" SNR single emitters in panels A and C are localized with less diffusivity, corresponding to

Table 2. Average error and precision of localized centroid position for simulated single emitters grouped by either SNR or blink rate.

Averaged by	$\|Err_x\|$ (nm)	s_x (nm)	$\|Err_y\|$ (nm)	s_y (nm)
High SNR	4.24	26.5	5.3	25.4
Low SNR	6.36	36.0	7.42	41.3
2 blinks/sec	5.3	31.8	6.36	34.0
3 blinks/sec	5.3	30.7	7.42	32.9

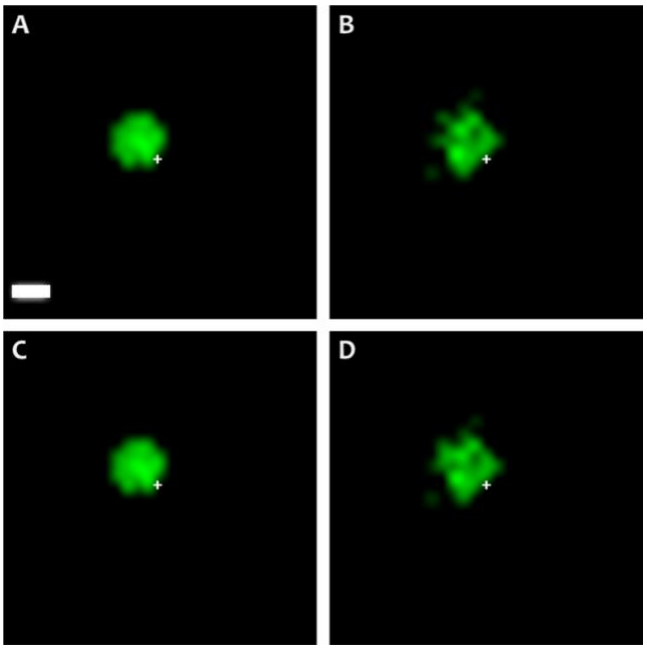

Figure 4. QuickPALM reconstruction outputs for the 1000-frame simulations of single emitters with the following parameters: A) High SNR&2bps, B) Low SNR & 2bps, C) High SNR & 3bps, D) Low SNR & 3bps. True positions marked by white crosses. Scale bar is 1 pixel (106nm).

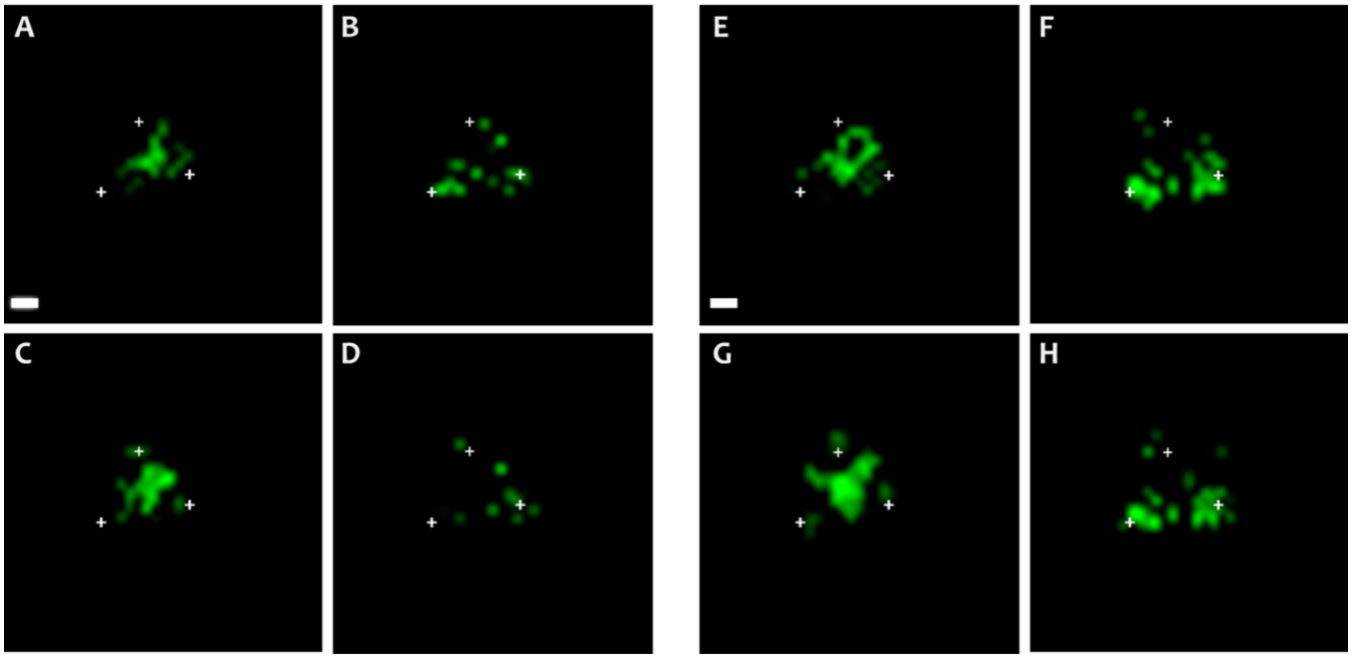

Figure 5. QuickPALM reconstruction outputs for the 1000 frame (A-D) and 3000 frame (E-H) overlapped multiple emitter simulations: A,E) High SNR & 2bps; B,F) Low SNR & 2bps; C,G) High SNR & 3bps; D,H) Low SNR & 3bps. True positions marked by white crosses. Scale bars are 1 pixel (106nm)

lower variance, compared to the simulations of "low" SNR single emitters in panels B and D. At first glance, the reconstruction image in panels B and D appear to overlay better with the true emitter positions. However, the majority of the localizations from QuickPALM, indicated by the brightest green spots, are farther away from the ground truth in panels B and D compared to panels A and C. This correlates with both the improved localization accuracy and precision when grouping by "high" vs "low" SNR in Table 2.

Interestingly, it was expected that increased blinking reduces the number of frames with a localized emitter and would result in a decreased precision, but no discernable difference in localization performance is observed when grouped solely by blink rate. Given that grouping simulations by blink rate averages over both "high" and "low" SNR emitters, it is likely that the increased localization precision from the "high" SNR simulations outweighs the loss of statistical precision from the reduced number of "on" frames at the higher blink rate. Note that in the single emitter case we did not explicitly parameterize for photostability. A more photostable emitter in a sparsely labeled scene is simply localized in more frames and as such reduces the localization error; this is noted in eq 1 by the inverse relationship between $\sigma_{x,y}$ and N, which is proportional to the number of "on" frames.

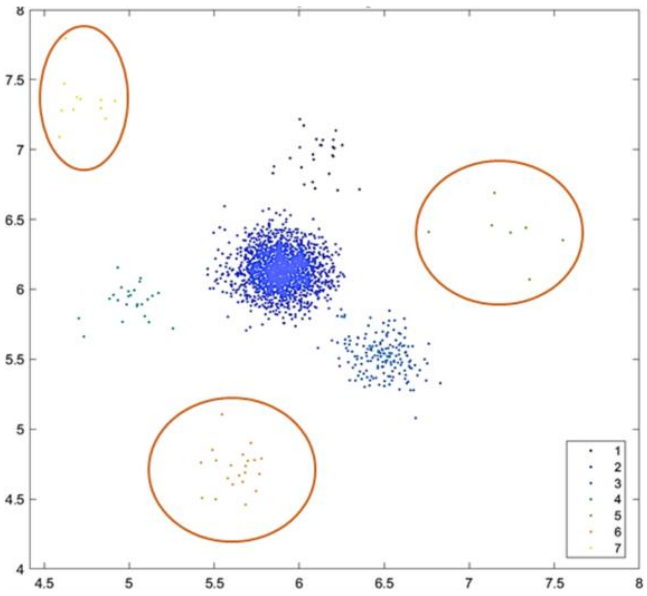

Figure 6. Hierarchical cluster analysis of QuickPALM localizations for multi-emitter simulations. Clusters associated with one of the three simulated emitters are traced by the orange circles.

To simulate more densely labeled samples typically used for STORM/PALM, movies were created with three adjacent emitters with overlapping point spread functions (PSFs). The three emitters within a simulated movie are generated using the same set of SNR and blink rate parameters (see Figure S21 for a diagram for how the emitters are overlapped). In this case, photostability should affect the number of frames in which a fluctuation in PL intensity, or blink, can occur that allows an emitter to be resolved from the others. Thus, we explicitly parameterized for photostability by creating a set of movies that are 1000 frames long and then another set that are 3000 frames long (Movies S6 and S7) and performed a similar set of analyses as performed on the single emitter simulations. The outputs from QuickPALM (Figure 5) were analyzed with a hierarchical clustering algorithm to identify clusters of localized points for each simulation that are associated with the true positions for each individual emitter, as circled in Figures 6. Further details about the cluster analysis are detailed in the SI. Clusters identified from the QuickPALM localizations that are not associated with the locations of the true emitters reflect regions where the PSFs from the

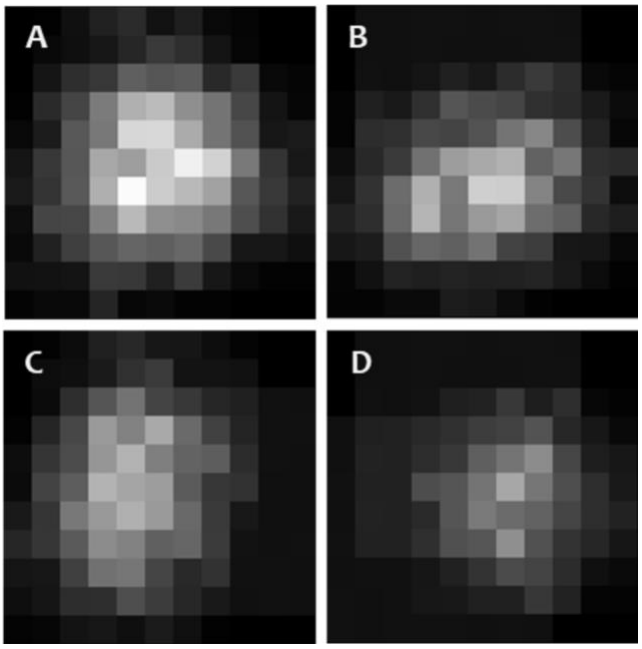

Figure 7. Select frames extracted from a simulation of multiple overlapped emitters where (A) all are on; (B,C) one of the emitters "blinked off" in the (B) top and (C) lower right; and (D) both the top and lower left emitters "blinked off" in the same frame.

individual emitters overlap. The large cluster in the center reflects the case where all emitters are on (Figures 6 and 7A) and the smaller clusters between the true positions result from localizations where only one of the emitters has blinked off (Figures 7B and C). Only when a single emitter is "on" in a densely labeled scene (Figure 7D) will the localization procedure result in a coordinate belonging to a cluster associated with one of the simulated true positions. The increased brightness at these superimposed regions biases the QuickPALM localization algorithm towards these pixels and are not associated with any of the ground truth positions. Thus, only clusters identified to be associated with one of the three simulated emitters are individually fitted with a 2D Gaussian to identify the centroid positions and associated localization error (see Figure S24, Tables S4 and S5). Like the single emitter scenario, the absolute error for the three overlapped emitters are grouped by SNR or blink rate to produce average centroid position and standard deviation within the same movie duration of either 1000 or 3000 frames (Table 3).

Table 3. Average error and precision for localized centroid positions in simulated overlapped emitters grouped by either SNR or blink rate.

1000-frame simulations				
Averaged by	$\lvert Err_x \rvert$ (nm)	s_x (nm)	$\lvert Err_y \rvert$ (nm)	s_y (nm)
High SNR	65.9	12.4	48.8	25.4
Low SNR	35.6	25.3	28.4	15.7
2 blinks/sec	49.2	20.6	43.9	26.3
3 blinks/sec	49.6	16.2	32.4	17.0
3000-frame simulations				
Averaged by	$\lvert Err_x \rvert$ (nm)	s_x (nm)	$\lvert Err_y \rvert$ (nm)	s_y (nm)
High SNR	30.4	20.2	20.8	21.7
Low SNR	33.6	12.7	22.5	12.7
2 blinks/sec	43.2	18.9	25.9	19.3
3 blinks/sec	22.9	12.6	18.3	13.4

The increased localization precision obtained from the 3000-frame movies (Figure 5E-H) compared to the 1000-frame movies (Figure 5A-D), regardless if grouped by SNR or blink rate, is expected; more frames means more opportunities to capture a stochastic blinking event that will allow adjacent emitters to be better resolved from one another. This is most apparent when comparing the number and intensity of green spots around the ground truth positions in panels C and D to those in panels G and H of Figure 5. Similarly, overlapped emitters that blink more frequently increase the probability of each frame missing at least one of the emitters to allow the remaining emitters to be resolved more accurately and precisely. Comparing the fitted centroids grouped by blink rate in both the 1000-frame and 3000-frame movies, the average error and average standard deviation of the fitted centroid positions are consistently lower at the faster blink rate 3bps. Unexpectedly, when grouping by SNR, simulations with emitters parameterized to high SNR result in a larger average error of the fitted centroid positions compared to those of low SNR. Based on localization accuracy the absolute errors from ground truth in the 3000-frame long simulations are similar when comparing high SNR and low SNR, but the precision of the localization is notably lower in the high SNR simulations. This deviation from the trend observed in the single emitter simulations seems counterintuitive; brighter emitters are expected to be easier to resolve. We theorize that the biasing of QuickPALM to the regions of overlap is further exacerbated by the excessively bright emitters; panels A,C,E and G exhibit more significant features in the regions between the ground truth positions compared to panels B,D,F and H in Figure 5.

Based on this, we find that localization precision in densely labeled scenes is dependent primarily on the blink rate and photostability of the emitter. This maximizes the number of observable blinking events, which reduces the number of overlapping of PSFs within a frame. Only after these individual emitters are reliably resolved from one another does the higher SNR, or brightness, positively contribute to the localization accuracy and precision. Without sufficient measurements where at least one of the emitters has "blinked" to an "off" state, the overlapped PSFs from emitters with high SNR biases localization algorithms towards the regions of overlap and greatly impacts both the accuracy and precision of SMLM measurements. Thus, the enhanced localization precision observed in the BKQDs when compared directly to TAMRA-BKs are likely the result of the faster, innate "blinking" and increased photostability of CdSe/CdS QDs.

QDs are expected to have enhanced localization precision compared to other fluorophores. While the CdSe/CdS QDs clearly outperform TAMRA, these results by

themselves provide no insight as to how QDs would compare to other fluorophores more commonly applied to single-molecule localization microscopy. To do so, we reference the work done by Dempsey et al.[79] that rigorously examined the differences in various photophysical parameters (i.e. survival fraction, switch rate, duty cycle) for fluorophores, such as TAMRA, routinely used for localization-based super-resolution techniques such as STORM. By normalizing these reported properties with respect to TAMRA, we extend the results of the computational analyses and simulations to predict how QD probes may perform in comparison to the other fluorophores. Specifically, we use the number of switching events, the survival fraction, and the brightness, defined as the product of the extinction coefficient ϵ and quantum yield QY, as a proxy for blink rate, photostability and SNR, respectively, to compare CdSe/CdS QDs to spectrally similar fluorophores (see Table S6). For example, comparing to AlexaFluor 647, considered as one of the most superior performing dyes for STORM experiments, we find that CdSe/CdS QDs are expected to blink 14% more, are 20% more photostable, and are on average 22% brighter, with respect to SNR. Note that values for the QD brightness are highly variable between different sizes and between different methods of synthesis for a given size. While the low end of the single QD brightness range is only a marginal improvement in brightness compared to AlexaFluor 647, our simulations have indicated that brightness is not a significant indicator of localization precision for a fluorophore in STORM/PALM experiments. Rather, the enhanced blinking and photostability of QDs will likely result in an improved accuracy and precision compared to all organic dyes, much like what we observed in the direct comparison to TAMRA.

CONCLUSION

Using fluorescence imaging of BKQDs bound to bradykinin receptors present on neurons and astrocytes as a model system, we find that as super-resolution imaging tools, QDs are superior probes to commonly used organic fluorophores. The inherent, fast blinking and extremely photostable fluorescence from individual QDs compared to organic dyes and fluorescent proteins provides for easier and more precise super-resolution localization in reconstructed images; blinking dictates the probability an individual emitter can be resolved from overlapped PSFs of nearby emitters and photostability increases the number of measurements, or frames, that a blink can occur in. Surprisingly, while we expected there to be significant dependence on the brightness, or SNR, of the individual emitter, we found that excessive brightness biases localization algorithms towards the overlapped regions of nearby emitters due to their superimposed brightness. Thus, while SNR does dictate the localization accuracy and precision of easily resolvable single emitters, its role is minor in well-labeled samples typical of STORM/PALM experiments. The broad absorption spectrum and intrinsic blinking nature of QD fluorescence also means that super-resolution imaging is relatively simple to employ. While QDs have long been touted as superior to organic fluorophores for conventional imaging applications,[31-34, 37, 39, 88-91] our results suggest that QDs should have substantial advantages over organic fluorophores for sub-diffraction limit imaging as well.

ASSOCIATED CONTENT

Supporting Information

The Supporting Information is available free of charge on the ACS Publications website.

Full experimental procedures, chemical structures, synthetic peptide and quantum dot characterization data, blinking traces, simulation data, and 30-day super-resolution results (PDF)

Custom-written scripts for computational analyses are available at the following github repository: https://github.com/wslchiang/QDvTAMRA

Movie S1. Blinking BKQDs bound to neuronal glial culture (.avi)

Movies S2-5. 1000-frame movie of single emitter simulation with: S2) High SNR & 2bps; S3) High SNR & 3bps; S4) Low SNR & 2bps; S5) Low SNR & 3bps (.mp4)

Movies S6 & S7. Simulation of multiple overlapped emitters for a duration of S6) 1000-frames and S7) 3000-frames (.mp4)

AUTHOR INFORMATION

Corresponding Authors

*krauss@chem.rochester.edu, nilsson@chem.rochester.edu, Harris_Gelbard@URMC.Rochester.edu.

Notes

The authors declare no competing financial interest.

ACKNOWLEDGMENT

This work was supported by the National Science Foundation (NSF) (CHE-1609365, CHE -1904847), NSF DMR-1148836, NIH R01HL138538 and NIH MH64570 (HAG) as well as the University of Rochester Sproull Fellowship (JMU). Additionally, this research was supported by a grant from the University of Rochester Center for AIDS Research (CFAR), an NIH-funded program (P30AI078498). The content is solely the responsibility of the authors and does not necessarily represent the official views of the National Institutes of Health.

REFERENCES

1. Huang, B.; Wang, W.; Bates, M.; Zhuang, X. Three-dimensional super-resolution imaging by stochastic optical reconstruction microscopy. *Science* **2008,** *319* (5864), 810-3.
2. Gallina, M. E.; Xu, J.; Dertinger, T.; Aizer, A.; Shav-Tal, Y.; Weiss, S. Resolving the spatial relationship between intracellular components by dual color super resolution optical fluctuations imaging (SOFI). *Opt Nanoscopy* **2013,** *2*.
3. Urban, B. E.; Xiao, L.; Dong, B.; Chen, S.; Kozorovitskiy, Y.; Zhang, H. F. Imaging neuronal structure dynamics using 2-photon super-resolution patterned excitation reconstruction microscopy. *J Biophotonics* **2018,** *11* (3).
4. Zeng, Z.; Chen, X.; Wang, H.; Huang, N.; Shan, C.; Zhang, H.; Teng, J.; Xi, P. Fast super-resolution imaging with ultra-high labeling density achieved by joint tagging super-resolution optical fluctuation imaging. *Sci Rep* **2015,** *5*, 8359.
5. Betzig, E.; Patterson, G. H.; Sougrat, R.; Lindwasser, O. W.; Olenych, S.; Bonifacino, J. S.; Davidson, M. W.; Lippincott-Schwartz, J.; Hess, H. F. Imaging intracellular fluorescent proteins at nanometer resolution. *Science* **2006,** *313* (5793), 1642-1645.
6. Hess, S. T.; Girirajan, T. P.; Mason, M. D. Ultra-high resolution imaging by fluorescence photoactivation localization microscopy. *Biophys J* **2006,** *91* (11), 4258-72.
7. Westphal, V.; Hell, S. W. Nanoscale resolution in the focal plane of an optical microscope. *Phys Rev Lett* **2005,** *94* (14), 143903.
8. Klar, T. A.; Engel, E.; Hell, S. W. Breaking Abbe's diffraction resolution limit in fluorescence microscopy with stimulated emission depletion beams of various shapes. *Phys Rev E Stat Nonlin Soft Matter Phys* **2001,** *64* (6 Pt 2), 066613.
9. Klar, T. A.; Jakobs, S.; Dyba, M.; Egner, A.; Hell, S. W. Fluorescence microscopy with diffraction resolution barrier broken by stimulated emission. *P Natl Acad Sci USA* **2000,** *97* (15), 8206-8210.
10. Rust, M. J.; Bates, M.; Zhuang, X. Sub-diffraction-limit imaging by stochastic optical reconstruction microscopy (STORM). *Nat Methods* **2006,** *3* (10), 793-5.
11. Almada, P.; Culley, S.; Henriques, R. PALM and STORM: Into large fields and high-throughput microscopy with sCMOS detectors. *Methods* **2015,** *88*, 109-21.
12. Hanne, J.; Falk, H. J.; Gorlitz, F.; Hoyer, P.; Engelhardt, J.; Sahl, S. J.; Hell, S. W. STED nanoscopy with fluorescent quantum dots. *Nat Commun* **2015,** *6*, 7127.
13. Leutenegger, M.; Eggeling, C.; Hell, S. W. Analytical description of STED microscopy performance. *Optics Express* **2010,** *18* (25), 26417.
14. Huang, B.; Babcock, H.; Zhuang, X. Breaking the diffraction barrier: super-resolution imaging of cells. *Cell* **2010,** *143* (7), 1047-58.
15. Gustafsson, M. G. L. Surpassing the lateral resolution limit by a factor of two using structured illumination microscopy. SHORT COMMUNICATION. *Journal of Microscopy* **2000,** *198* (2), 82-87.
16. Huang, B. Super-resolution optical microscopy: multiple choices. *Curr Opin Chem Biol* **2010,** *14* (1), 10-4.
17. Sigal, Y. M.; Zhou, R. B.; Zhuang, X. W. Visualizing and discovering cellular structures with super-resolution microscopy. *Science* **2018,** *361* (6405), 880-887.
18. Owen, D. M.; Magenau, A.; Williamson, D. J.; Gaus, K. Super-resolution imaging by localization microscopy. *Methods Mol Biol* **2013,** *950*, 81-93.
19. Kamiyama, D.; Huang, B. Development in the STORM. *Dev Cell* **2012,** *23* (6), 1103-10.
20. Thompson, M. A.; Biteen, J. S.; Lord, S. J.; Conley, N. R.; Moerner, W. E., Molecules and Methods for Super-Resolution Imaging. In *Single Molecule Tools, Part B:Super-Resolution, Particle Tracking, Multiparameter, and Force Based Methods*, 2010; pp 27-59.
21. Pereira, P. M.; Almada, P.; Henriques, R. High-content 3D multicolor super-resolution localization microscopy. *Methods Cell Biol* **2015,** *125*, 95-117.
22. Waldchen, S.; Lehmann, J.; Klein, T.; van de Linde, S.; Sauer, M. Light-induced cell damage in live-cell super-resolution microscopy. *Sci Rep* **2015,** *5*, 15348.
23. Liu, Y.; Lu, Y.; Yang, X.; Zheng, X.; Wen, S.; Wang, F.; Vidal, X.; Zhao, J.; Liu, D.; Zhou, Z., et al. Amplified stimulated emission in upconversion nanoparticles for super-resolution nanoscopy. *Nature* **2017,** *543* (7644), 229-233.
24. Zhan, Q.; Liu, H.; Wang, B.; Wu, Q.; Pu, R.; Zhou, C.; Huang, B.; Peng, X.; Ågren, H.; He, S. Achieving high-efficiency emission depletion nanoscopy by employing cross relaxation in upconversion nanoparticles. *Nature Communications* **2017,** *8* (1), 1058.
25. Arroyo-Camejo, S.; Adam, M.-P.; Besbes, M.; Hugonin, J.-P.; Jacques, V.; Greffet, J.-J.; Roch, J.-F.; Hell, S. W.; Treussart, F. Stimulated Emission Depletion Microscopy Resolves Individual Nitrogen Vacancy Centers in Diamond Nanocrystals. *ACS Nano* **2013,** *7* (12), 10912-10919.
26. Laporte, G.; Psaltis, D. STED imaging of green fluorescent nanodiamonds containing nitrogen-vacancy-nitrogen centers. *Biomed Opt Express* **2015,** *7* (1), 34-44.
27. Fang, X.; Chen, X.; Li, R.; Liu, Z.; Chen, H.; Sun, Z.; Ju, B.; Liu, Y.; Zhang, S. X.-A.; Ding, D., et al. Multicolor Photo-Crosslinkable AIEgens toward Compact Nanodots for Subcellular Imaging and STED Nanoscopy. *Small* **2017,** *13* (41), 1702128.
28. Li, D.; Qin, W.; Xu, B.; Qian, J.; Tang, B. Z. AIE Nanoparticles with High Stimulated Emission Depletion Efficiency and Photobleaching Resistance for Long-Term Super-Resolution Bioimaging. *Advanced Materials* **2017,** *29* (43), 1703643.
29. Khan, S.; Verma, N. C.; Gupta, A.; Nandi, C. K. Reversible Photoswitching of Carbon Dots. *Scientific Reports* **2015,** *5* (1), 11423.
30. Chen, X.; Li, R.; Liu, Z.; Sun, K.; Sun, Z.; Chen, D.; Xu, G.; Xi, P.; Wu, C.; Sun, Y. Small Photoblinking Semiconductor Polymer Dots for Fluorescence Nanoscopy. *Advanced Materials* **2017,** *29* (5), 1604850.
31. Bruchez Jr, M. Semiconductor Nanocrystals as Fluorescent Biological Labels. *Science* **1998,** *281* (5385), 2013-2016.
32. Dahan, M.; Laurence, T.; Pinaud, F.; Chemla, D. S.; Alivisatos, A. P.; Sauer, M.; Weiss, S. Time-gated biological imaging by use of colloidal quantum dots. *Optics Letters* **2001,** *26* (11), 825.
33. Michalet, X.; Pinaud, F.; Lacoste, T. D.; Dahan, M.; Bruchez, M. P.; Alivisatos, A. P.; Weiss, S. Properties of Fluorescent Semiconductor Nanocrystals and their Application to Biological Labeling. *Single Molecules* **2001,** *2* (4), 261-276.
34. Chan, W. C. W.; Maxwell, D. J.; Gao, X.; Bailey, R. E.; Han, M.; Nie, S. Luminescent quantum dots for multiplexed biological detection and imaging. *Current Opinion in Biotechnology* **2002,** *13* (1), 40-46.
35. Gao, X.; Nie, S. Molecular profiling of single cells and tissue specimens with quantum dots. *Trends in Biotechnology* **2003,** *21* (9), 371-373.
36. Byers, R. J.; Hitchman, E. R. Quantum dots brighten biological imaging. *Prog Histochem Cytochem* **2011,** *45* (4), 201-37.
37. Jaiswal, J. K.; Simon, S. M. Potentials and pitfalls of fluorescent quantum dots for biological imaging. *Trends Cell Biol* **2004,** *14* (9), 497-504.
38. Bruchez, M. P. Turning all the lights on: quantum dots in cellular assays. *Curr Opin Chem Biol* **2005,** *9* (5), 533-7.
39. Martynenko, I. V.; Litvin, A. P.; Purcell-Milton, F.; Baranov, A. V.; Fedorov, A. V.; Gun'ko, Y. K. Application of semiconductor quantum dots in bioimaging and biosensing. *Journal of Materials Chemistry B* **2017,** *5* (33), 6701-6727.
40. Yang, X.; Zhanghao, K.; Wang, H.; Liu, Y.; Wang, F.; Zhang, X.; Shi, K.; Gao, J.; Jin, D.; Xi, P. Versatile Application of Fluorescent Quantum Dot Labels in Super-resolution Fluorescence Microscopy. *ACS Photonics* **2016,** *3* (9), 1611-1618.
41. Wang, Y.; Fruhwirth, G.; Cai, E.; Ng, T.; Selvin, P. R. 3D super-resolution imaging with blinking quantum dots. *Nano Lett* **2013,** *13* (11), 5233-41.
42. Xu, J.; Tehrani, K. F.; Kner, P. Multicolor 3D super-resolution imaging by quantum dot stochastic optical reconstruction microscopy. *ACS Nano* **2015,** *9* (3), 2917-25.
43. Mandula, O.; Sestak, I. S.; Heintzmann, R.; Williams, C. K. Localisation microscopy with quantum dots using non-negative matrix factorisation. *Opt Express* **2014,** *22* (20), 24594-605.

44. Hahn, M. A.; Tabb, J. S.; Krauss, T. D. Detection of single bacterial pathogens with semiconductor quantum dots. *Anal Chem* **2005,** *77* (15), 4861-9.
45. Dertinger, T.; Colyer, R.; Iyer, G.; Weiss, S.; Enderlein, J. Fast, background-free, 3D super-resolution optical fluctuation imaging (SOFI). *Proc Natl Acad Sci U S A* **2009,** *106* (52), 22287-92.
46. Watanabe, T. M.; Fukui, S.; Jin, T.; Fujii, F.; Yanagida, T. Real-time nanoscopy by using blinking enhanced quantum dots. *Biophys J* **2010,** *99* (7), L50-2.
47. Xu, J.; Fan, Q.; Mahajan, K. D.; Ruan, G.; Herrington, A.; Tehrani, K. F.; Kner, P.; Winter, J. O. Micelle-templated composite quantum dots for super-resolution imaging. *Nanotechnology* **2014,** *25* (19), 195601.
48. Hoyer, P.; Staudt, T.; Engelhardt, J.; Hell, S. W. Quantum dot blueing and blinking enables fluorescence nanoscopy. *Nano Lett* **2011,** *11* (1), 245-50.
49. Song, M.; Karatutlu, A.; Ali, I.; Ersoy, O.; Zhou, Y.; Yang, Y.; Zhang, Y.; Little, W. R.; Wheeler, A. P.; Sapelkin, A. V. Spectroscopic super-resolution fluorescence cell imaging using ultra-small Ge quantum dots. *Opt Express* **2017,** *25* (4), 4240-4253.
50. Jung, S.; Park, J.; Bang, J.; Kim, J. Y.; Kim, C.; Jeon, Y.; Lee, S. H.; Jin, H.; Choi, S.; Kim, B., et al. Light-Induced Fluorescence Modulation of Quantum Dot-Crystal Violet Conjugates: Stochastic Off-On-Off Cycles for Multicolor Patterning and Super-Resolution. *J Am Chem Soc* **2017,** *139* (22), 7603-7615.
51. Eremchev, I. Y.; Lozing, N. A.; Baev, A. A.; Tarasevich, A. O.; Gladush, M. G.; Rozhentsov, A. A.; Naumov, A. V. Luminescence Microscopy of Single Quantum Dot Pairs with Nanometer Spatial Resolution. *JETP Letters* **2018,** *108* (1), 30-37.
52. Chien, F. C.; Kuo, C. W.; Chen, P. Localization imaging using blinking quantum dots. *Analyst* **2011,** *136* (8), 1608-13.
53. Lee, L. Y.; Ong, S. L.; Hu, J. Y.; Ng, W. J.; Feng, Y.; Tan, X.; Wong, S. W. Use of semiconductor quantum dots for photostable immunofluorescence labeling of Cryptosporidium parvum. *Appl Environ Microbiol* **2004,** *70* (10), 5732-6.
54. Chinnathambi, S.; Hanagata, N. Photostability of quantum dot micelles under ultraviolet irradiation. *Luminescence* **2019,** *34* (5), 472-479.
55. Hoshino, A.; Manabe, N.; Fujioka, K.; Suzuki, K.; Yasuhara, M.; Yamamoto, K. Use of fluorescent quantum dot bioconjugates for cellular imaging of immune cells, cell organelle labeling, and nanomedicine: surface modification regulates biological function, including cytotoxicity. *J Artif Organs* **2007,** *10* (3), 149-57.
56. Lichtman, J. W.; Conchello, J. A. Fluorescence microscopy. *Nat Methods* **2005,** *2* (12), 910-9.
57. Medintz, I. L.; Uyeda, H. T.; Goldman, E. R.; Mattoussi, H. Quantum dot bioconjugates for imaging, labelling and sensing. *Nat Mater* **2005,** *4* (6), 435-46.
58. Nirmal, M.; Dabbousi, B. O.; Bawendi, M. G.; Macklin, J. J.; Trautman, J. K.; Harris, T. D.; Brus, L. E. Fluorescence intermittency in single cadmium selenide nanocrystals. *Nature* **1996,** *383* (6603), 802-804.
59. Liu, L.; Mirandola, L.; Chiriva-Internati, M.; Chaudhuri, J. CdS quantum dot-chitosan-anti SP17 nanohybrid as a potential cancer biomarker. *Materials Letters* **2017,** *199*, 5-8.
60. George, J.; Ganapathy, S.; Muthusamy, G. Quantum Dots as Fluorescent Dyes for Imaging of Melanoma Cells: Sound Contribution of Nanotechnology to Biological Science. *Journal of Bionanoscience* **2016,** *10* (3), 205-210.
61. Trapiella-Alfonso, L.; Pons, T.; Lequeux, N.; Leleu, L.; Grimaldi, J.; Tasso, M.; Oujagir, E.; Seguin, J.; d'Orlye, F.; Girard, C., et al. Clickable-Zwitterionic Copolymer Capped-Quantum Dots for in Vivo Fluorescence Tumor Imaging. *ACS Appl Mater Interfaces* **2018,** *10* (20), 17107-17116.
62. Wang, J.; Wang, F.; Li, F.; Zhang, W.; Shen, Y.; Zhou, D.; Guo, S. A multifunctional poly(curcumin) nanomedicine for dual-modal targeted delivery, intracellular responsive release, dual-drug treatment and imaging of multidrug resistant cancer cells. *J Mater Chem B* **2016,** *4* (17), 2954-2962.
63. McHugh, K. J.; Jing, L.; Behrens, A. M.; Jayawardena, S.; Tang, W.; Gao, M.; Langer, R.; Jaklenec, A. Biocompatible Semiconductor Quantum Dots as Cancer Imaging Agents. *Adv Mater* **2018,** *30* (18), e1706356.
64. Delehanty, J. B.; Susumu, K.; Manthe, R. L.; Algar, W. R.; Medintz, I. L. Active cellular sensing with quantum dots: transitioning from research tool to reality; a review. *Anal Chim Acta* **2012,** *750*, 63-81.
65. Susumu, K.; Field, L. D.; Oh, E.; Hunt, M.; Delehanty, J. B.; Palomo, V.; Dawson, P. E.; Huston, A. L.; Medintz, I. L. Purple-, Blue-, and Green-Emitting Multishell Alloyed Quantum Dots: Synthesis, Characterization, and Application for Ratiometric Extracellular pH Sensing. *Chemistry of Materials* **2017,** *29* (17), 7330-7344.
66. Wang, G.; Li, Z.; Ma, N. Next-Generation DNA-Functionalized Quantum Dots as Biological Sensors. *ACS Chem Biol* **2018,** *13* (7), 1705-1713.
67. Bruchez, M. P. Quantum dots find their stride in single molecule tracking. *Curr Opin Chem Biol* **2011,** *15* (6), 775-80.
68. Bannai, H. Molecular membrane dynamics: Insights into synaptic function and neuropathological disease. *Neurosci Res* **2018,** *129*, 47-56.
69. Jonas, M.; Yao, Y.; So, P. T. C.; Dewey, C. F. Detecting Single Quantum Dot Motion With Nanometer Resolution for Applications in Cell Biology. *IEEE Transactions on Nanobioscience* **2006,** *5* (4), 246-250.
70. Liu, Y.; Oda, H.; Inoue, Y.; Ishihara, K. Movement of a Quantum Dot Covered with Cytocompatible and pH-Responsible Phospholipid Polymer Chains under a Cellular Environment. *Biomacromolecules* **2016,** *17* (12), 3986-3994.
71. Cai, E.; Ge, P.; Lee, S. H.; Jeyifous, O.; Wang, Y.; Liu, Y.; Wilson, K. M.; Lim, S. J.; Baird, M. A.; Stone, J. E., et al. Stable small quantum dots for synaptic receptor tracking on live neurons. *Angew Chem Int Ed Engl* **2014,** *53* (46), 12484-8.
72. Wichner, S. M.; Mann, V. R.; Powers, A. S.; Segal, M. A.; Mir, M.; Bandaria, J. N.; DeWitt, M. A.; Darzacq, X.; Yildiz, A.; Cohen, B. E. Covalent Protein Labeling and Improved Single-Molecule Optical Properties of Aqueous CdSe/CdS Quantum Dots. *ACS Nano* **2017,** *11* (7), 6773-6781.
73. Kress, S. J.; Antolinez, F. V.; Richner, P.; Jayanti, S. V.; Kim, D. K.; Prins, F.; Riedinger, A.; Fischer, M. P.; Meyer, S.; McPeak, K. M., et al. Wedge Waveguides and Resonators for Quantum Plasmonics. *Nano Lett* **2015,** *15* (9), 6267-75.
74. Kress, S. J.; Richner, P.; Jayanti, S. V.; Galliker, P.; Kim, D. K.; Poulikakos, D.; Norris, D. J. Near-field light design with colloidal quantum dots for photonics and plasmonics. *Nano Lett* **2014,** *14* (10), 5827-33.
75. Solutions, L. L. S. Protocol: Maleimide labeling of proteins and other thiolated biomolecules. https://www.lumiprobe.com/protocols/protein-maleimide-labeling.
76. Hermanson, G. T., *Bioconjugate Techniques*. 3rd ed.; Elsevier: Amsterdam, 2013.
77. Maiseyeu, A.; Bagalkot, V. In vitro uptake of apoptotic body mimicking phosphatidylserine-quantum dot micelles by monocytic cell line. *Nanoscale Res Lett* **2014,** *9* (1), 176.
78. van de Linde, S.; Loschberger, A.; Klein, T.; Heidbreder, M.; Wolter, S.; Heilemann, M.; Sauer, M. Direct stochastic optical reconstruction microscopy with standard fluorescent probes. *Nat Protoc* **2011,** *6* (7), 991-1009.
79. Dempsey, G. T.; Vaughan, J. C.; Chen, K. H.; Bates, M.; Zhuang, X. Evaluation of fluorophores for optimal performance in localization-based super-resolution imaging. *Nat Methods* **2011,** *8* (12), 1027-36.
80. Henriques, R.; Lelek, M.; Fornasiero, E. F.; Valtorta, F.; Zimmer, C.; Mhlanga, M. M. QuickPALM: 3D real-time photoactivation nanoscopy image processing in ImageJ. *Nat Methods* **2010,** *7* (5), 339-40.
81. Endesfelder, U.; Heilemann, M. Direct stochastic optical reconstruction microscopy (dSTORM). *Methods Mol Biol* **2015,** *1251*, 263-76.
82. Allen, J. R.; Ross, S. T.; Davidson, M. W. Single molecule localization microscopy for superresolution. *Journal of Optics* **2013,** *15* (9).
83. de Weerd, W. F.; Leeb-Lundberg, L. M. Bradykinin sequesters B2 bradykinin receptors and the receptor-coupled Galpha subunits Galphaq and Galphai in caveolae in DDT1 MF-2 smooth muscle cells. *J Biol Chem* **1997,** *272* (28), 17858-66.

84. AbdAlla, S.; Zaki, E.; Lother, H.; Quitterer, U. Involvement of the amino terminus of the B(2) receptor in agonist-induced receptor dimerization. *J Biol Chem* **1999,** *274* (37), 26079-84.
85. Yang, L.; Scarlata, S. Super-resolution Visualization of Caveola Deformation in Response to Osmotic Stress. *J Biol Chem* **2017,** *292* (9), 3779-3788.
86. Pike, L. J. Lipid rafts: bringing order to chaos. *J Lipid Res* **2003,** *44* (4), 655-67.
87. Fallahi-Sichani, M.; Linderman, J. J. Lipid raft-mediated regulation of G-protein coupled receptor signaling by ligands which influence receptor dimerization: a computational study. *PLoS One* **2009,** *4* (8), e6604.
88. Klostranec, J. M.; Chan, W. C. W. Quantum Dots in Biological and Biomedical Research: Recent Progress and Present Challenges. *Advanced Materials* **2006,** *18* (15), 1953-1964.
89. Resch-Genger, U.; Grabolle, M.; Cavaliere-Jaricot, S.; Nitschke, R.; Nann, T. Quantum dots versus organic dyes as fluorescent labels. *Nat Methods* **2008,** *5* (9), 763-75.
90. Gao, X.; Chan, W. C.; Nie, S. Quantum-dot nanocrystals for ultrasensitive biological labeling and multicolor optical encoding. *J Biomed Opt* **2002,** *7* (4), 532-537.
91. Taylor, J. R.; Fang, M. M.; Nie, S. Probing specific sequences on single DNA molecules with bioconjugated fluorescent nanoparticles. *Anal Chem* **2000,** *72* (9), 1979-86.

TOC Graphic: